Materials Advances

ROYAL SOCIETY OF CHEMISTRY

PAPER

View Article Online
View Journal | View Issue

Cite this: *Mater. Adv.*, 2021, **2**, 1043

A reversible and fast-responsive humidity sensor based on a lead-free Cs_2TeCl_6 double perovskite†

Chaojie Pi,[ab] Xue Yu,[a] Weiqing Chen,[a] Liuli Yang,[a] Chao Wang,[a] Zhichao Liu,[a] Yiya Wang,[b] Jianbei Qiu,[a] Bitao Liu *[ab] and Xuhui Xu *[a]

Received 26th October 2020,
Accepted 27th December 2020

DOI: 10.1039/d0ma00835d

rsc.li/materials-advances

Owing to their high conductivity and carrier mobility, the outstanding achievements of lead halide perovskites have been demonstrated in humidity sensor applications. However, the rapid degradation of perovskites upon over-exposure to high humidity as well as the toxicity of lead hinder their large-scale commercial applications. Herein, a lead-free Cs_2TeCl_6 double perovskite is explored to detect humidity owing to its extraordinary humidity-dependent electrical properties. The Cs_2TeCl_6 thin film explored as a perovskite-based humidity sensor shows excellent reliability and stability in relative humidity (RH) range from 5% to 90% with a super-fast response (13.8 s) and recovery time (1.39 s). Moreover, the outstanding reversible ability of the developed sensor was achieved when the humidity detector was repaired using HCl gas, thus overcoming the inevitable degradation issue of the perovskite-based sensors, even working in a long-term humidity environment (RH > 90%). Furthermore, the integrated Cs_2TeCl_6 perovskite-based face mask was used for the real-time monitoring of human respiration, giving a basic human assessment of health status directly and rapidly.

Introduction

Humidity sensing devices have attracted tremendous attention for their potential applications covering health monitoring, weather forecast, agricultural fields, and aerospace exploration.[1–4] Metal oxides, photonic crystals, polymer materials, and graphene composites have been employed as detection materials;[5–12] unfortunately, the complicated synthesis procedures, low sensitivity, and limited operating range contribute to an urgent demand for exploring more reliable, responsive and commercial humidity-sensing materials. Compared with available candidates, organic/inorganic perovskites greatly appear to be attractive and competitive potential materials due to their high sensitivity, simple fabrication process, and excellent physical properties (*e.g.*, high conductivity, high carrier mobility, and tenable bandgap). Hu *et al.*[13] reported $CH_3NH_3PbI_{3-x}Cl_x$ films as a humidity sensor for detecting relative humidity (RH) range from 32 to 97% with a recovery time of 74 s. Furthermore, a $CH_3NH_3PbBr_3$ humidity sensor with a wider humidity detection range (7–98%), high sensitivity and fast response (250 s), and recovery time (30–70 s) were investigated.[14] Subsequently, Ren *et al.*[15] demonstrated the excellent moisture sensitivity of the vertically aligned nanosheet arrays of $CH_3NH_3PbI_{3-x}Cl_x$, which show strong stability against decomposition by water molecules. Moreover, the correspondingly developed device exhibits a faster response time than the commercially available psychrometer, reaching the first RH peak in 21 s, compared to 51 s by the commercial counterpart. Although considerable efforts have been made, lead toxicity and the inevitable device degradation in the humidity environment (RH > 90%) of the involved perovskite-based sensor remains a daunting challenge.[16–21] The degradation of organic/inorganic perovskites is determined by the low formation energy and inherent structural instability, which can easily cause crystal structure damage, phase separation, and precipitation of the heavy metal element lead.[22,23]

Herein, a full inorganic lead-free and stable Cs_2TeCl_6 perovskite, which is a vacancy-ordered structure with isolated $[TeCl_6]^{2-}$ octahedral, was explored *via* a wet-chemical process. Moreover, the Cs_2TeCl_6 thin film, as a perovskite-based humidity sensor, exhibits a promising humidity detection ability with an outstanding reversible property due to its special structure. A fast response time could be achieved for the designed humidity sensor causing a facile repair process and overcoming the degradation issue of the perovskite-based sensor, even working in a long-term high humidity environment (RH > 90%). Owing to its good stability, superfast response and recovery ability, the explored Cs_2TeCl_6-based humidity sensor is integrated into a portable mask, providing the real-time assessment of human respiration with high-performance.

[a] College of Materials Science and Engineering, Kunming University of Science and Technology, Kunming 650093, P. R. China. E-mail: xuxuh07@126.com
[b] Research Institute for New Materials Technology, Chongqing University of Arts and Sciences, Chongqing 402160, P. R. China. E-mail: liubitao007@163.com

† Electronic supplementary information (ESI) available. See DOI: 10.1039/d0ma00835d

Results and discussion

We investigated the structural properties of the Cs_2TeCl_6 perovskite particles *via* X-ray diffraction (XRD). All the diffraction patterns match well with the standard patterns of Cs_2TeCl_6 (JCPDS No. 75-0377) shown in Fig. 1a, and the XRD refinement shown in Fig. 1b ensured that the pure phase was derived for the Cs_2TeCl_6 perovskite. The inset is the crystal structure of Cs_2TeCl_6, which belongs to the *Fm*3*m* space group (a = 10.449 Å) and adopts a vacancy-ordered structure with isolated $[TeCl_6]^{2-}$ octahedra.[24] The scanning electron microscopy (SEM) image (Fig. 1c) shows that the mean particle size is 7–10 μm, and the energy dispersive spectroscopy (EDS) mapping demonstrates the uniform distribution of the Cs, Te, and Cl elements, with the atomic ratio of Cs : Te : Cl being close to 2 : 1 : 6 (Fig. S1, ESI†), which is consistent with the XRD results. As shown in Fig. 1d, the density functional theory (DFT) calculation results show that Cs_2TeCl_6 has an indirect bandgap with a bandgap of 2.546 eV, and the electronic structure of the valence band originates predominantly from Cs 2p states, whereas the conduction band is composed mostly of Te 4s and Cl 2p states as inferred from the partial density of state (PDOS) information shown in Fig. S2 (ESI†). Cs_2TeCl_6 exhibits yellow emission centered at 595 nm with a long lifetime of 206 ns at room temperature (Fig. 1e and f). Its absorption edge is located at 495 nm, which is consistent with the DFT calculation.

We investigated the performance of the humidity detection ability by building a sensing setup, where the relative data were acquired in a clean-room with an ambient temperature of 30 °C (Fig. 2a). The as-developed Cs_2TeCl_6 thin film as a sensor (Fig. 2b) was placed into a hermetic metallic conduit with three through-holes for the dry and wet air inlets and outlets. The RH in the metallic conduit was controlled by a mass flow controller (MFC) to flow the wet or dry air gas into the testing chamber, and the RH value in the tube could be read from a commercial humidity sensor. Notably, we observe the reversible operation of the Cs_2TeCl_6-based device when exposed in the RH range from 5 to 90% (Fig. 2c). The developed humidity sensor device exhibits extraordinary humidity-dependent electrical properties

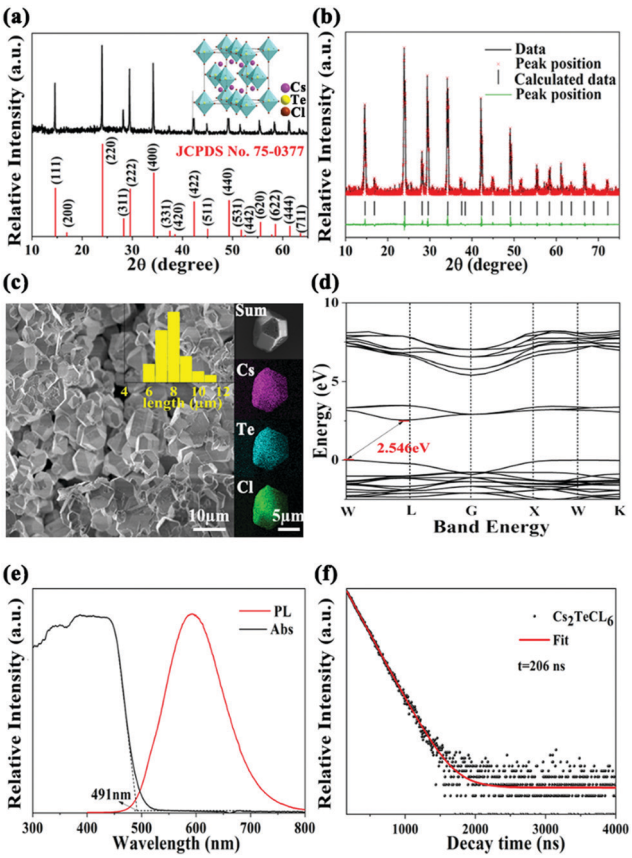

Fig. 1 (a) XRD patterns of the as-obtained Cs_2TeCl_6 and the inset is the schematic structure of Cs_2TeCl_6. (b) Rietveld XRD refinement results of Cs_2TeCl_6 using the MAUD refinement program. The black solid lines and red crosses are the experimental and calculated patterns, respectively, while the black short vertical lines represent the positions of the Bragg diffractions of the calculated patterns. The difference between the experimental and calculated patterns is plotted as the chartreuse line. The reliability parameters of the refinement are R_b = 10.50%, R_{wp} = 13.13%, and x^2 = 1.876. (c) SEM and EDS mapping images of Cs, Te, Cl elements of the Cs_2TeCl_6 samples, and the inset is the particle size distribution graph. (d) Calculated band structure of Cs_2TeCl_6. (e) PL and absorption spectra, and (f) time-resolved PL decay spectrum of the as-obtained Cs_2TeCl_6 at room temperature.

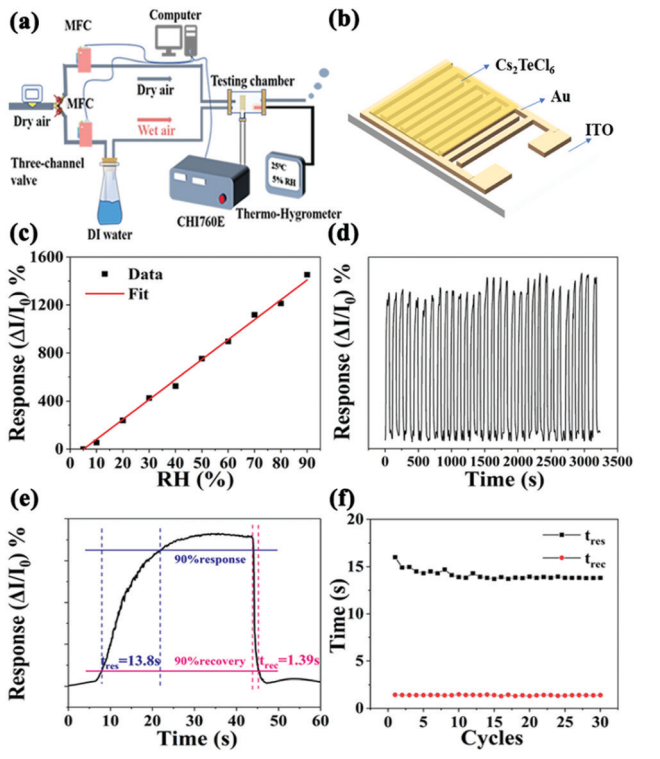

Fig. 2 The dynamic response and recovery characterization of the Cs_2TeCl_6-based humidity sensor. (a) Schematic of the real-time humidity sensing setup; (b) schematic of the device structure of the Cs_2TeCl_6 thin film humidity sensor; (c) the response and recovery curves of Cs_2TeCl_6 at various RH levels; (d) the dynamic response and recovery curve for 30 cycles measured under 0.1 V bias; (e) one dynamic response and recovery curve under 0.1 V bias; (f) the recorded response and recovery times of the Cs_2TeCl_6-based humidity sensor with different measuring cycles.

in the RH ranging from 5 to 90%. Moreover, the dynamic response and recovery curve of the Cs_2TeCl_6 humidity sensor for 30 cycles under a bias of 0.1 V at 90% RH are shown in Fig. 2d. The results confirm that the developed humidity sensor possesses superior repeatability and reliability in a continuous measurement (RH: 90%). The response and recovery times from the sensing curves are extrapolated, as illustrated in Fig. 2e. The response (t_{res}) and recovery time (t_{rec}) are defined as the time needed to attain 90% of $\Delta I(I - I_0)$, where I_0 is the initial current, which in the present case is taken as the value at 5% RH, and I is the current measured at different RH levels.[25] Hence, the humidity sensor exhibits an ultra-fast response and recovery time of 13.8 and 1.39 s, respectively, which are mainly due to the planar structure, where the water molecules can be easily volatilized during the desorption process.[26] In addition, the bond between the Cs_2TeCl_6 thin film surface and water molecules is relatively weaker than that on the metal oxide ceramics humidity sensor since the hydrogen bond H–Cl is weaker than H–O. As a result, it could be easier for the first-layer water molecules to volatilize from the Cs_2TeCl_6 film surface than from the metal oxide ceramic surface. The performance of which is superior to that of the reported available humidity sensors listed in Table 1 to the best of our knowledge. Particularly, the recovery speed is extremely noticeable surpassing that of the reported perovskite-based humidity sensors.[14,15,27–33] In fact, the stability of the humidity sensor is determined by the performance of the explored Cs_2TeCl_6 perovskite. The long-term performance of the Cs_2TeCl_6-based humidity sensor in the RH range of 5 to 90% was investigated. As shown in the PL spectra in Fig. S3 (ESI†), Cs_2TeCl_6 particles still maintain 85% of the initial luminescence intensity after being placed in an ambient environment at room temperature with an RH of 50% for 45 days. In addition, XRD results (Fig. S4, ESI†) confirmed the stability of the as-obtained Cs_2TeCl_6 humidity sensor, as seen from the original XRD patterns of Cs_2TeCl_6 exhibited insignificant changes after being placed at room temperature for 45 days. The TG and DSC curves in Fig. S5 (ESI†) characterize its thermodynamic properties, which suggests that Cs_2TeCl_6 could be stabilized below 400 °C. The above results prove the unique and stable crystal structure of the explored Cs_2TeCl_6 in the humidity range (5–90%). As shown in Fig. 2f, the response and recovery time hardly changed with the increased cycles, which proves the excellent stability of the explored Cs_2TeCl_6-based sensor.

Normalized sensitivity (S) is a significant parameter for a humidity sensor, which is defined as $S = |R_x - R_0|/R_0$. R_x and R_0 refer to resistances at x% and 5% RH, respectively.[34] The resistance of the sensor can be obtained from the linear fitting of the I–V curves. Hence, the I–V (current–voltage) curves of the sensor are measured in a climatic chamber, and the result shows a continuous increase in the current response with the increase in the RH value, as shown in Fig. 3a. Moreover, the relationship between the current and the RH values is recorded when the sensor is biased at the voltage of 5 V, and the result of which is plotted in the inset of Fig. 3a. It shows that the current in the humidity sensor grows exponentially with the increased RH value. As the humidity increases from 5 to 90%, the resistance of the sensors decreases from 10^{11} to 10^8 Ω. The sensitivity of the humidity sensor is determined to be 984. Besides, there is an abrupt increase in current when the humidity increases from 50 to 67% RH, as shown in the logarithmic representation shown in Fig. 3b, which indicates that moisture absorption is enhanced in this humidity range. These results demonstrate that the resistance shows an excellent logarithmic linearity toward RH. It has been reported that heat treatment can facilitate the degradation process of the perovskite under humidity condition.[35–37] Hence, we monitored the sensor resistance at 30 °C, 40 °C, and 50 °C, as shown in Fig. 3c. It can be seen that the resistance of the humidity sensor decreases with the increase in temperature from 30 to 50 °C, which can be attributed to the larger saturated water vapor pressure at 50 °C. Fig. 3d shows that the resistance of the device decreases significantly with the increase in humidity, which is consistent with the result of the CV curve shown in Fig. 3a. Notably, the resistance value of the humidity sensor hardly changed, which indicates the long-term stability of the device. However, after Cs_2TeCl_6 was treated at ultra-high humidity (RH = 100%), as shown in Fig. S6 (ESI†), it was found that a small impurity peak of $H_2Te_2O_6$ appeared, although the main diffraction peak of XRD still existed. Moreover, Cs_2TeCl_6 and a very small amount of CsCl raw material phase of the above-involved perovskite appears after treatment at 70 °C, suggesting that the damaged Cs_2TeCl_6 in a high humidity environment (RH > 90%) could be repaired to some extent. The PL emission spectra shown in Fig. S8 (ESI†) further confirmed the above conclusion. The sample that was immersed in water exhibited characteristic yellow-green luminescence again, with a much weaker luminous intensity compared to the original luminous

Table 1 Comparison of the response/recovery times of numerous humidity sensors

Type	Fabrication	Measure range (%)	t_{res} (s)	t_{rec} (s)	Ref.
$CH_3NH_3PbBr_3$	Grinding	7–98	250	30–70	Xu *et al.*[14]
$CH_3NH_3PbI_{0.2}Cl_{2.8}$	Solution growth	35–65	24	24	Ren *et al.*[15]
$Cs_2BiAgBr_6$ film	Spin-coating	5–75	1.78	0.45	Weng *et al.*[26]
$CdTiO_3$ nanofibers	Electrospinning	40–90	4	6	Imran *et al.*[27]
$ZnSnO_3$	Hydrothermal	11–97	7	16	Bauskar *et al.*[28]
$K_{0.5}Na_{0.5}NbO_3$	MOD	11–95	8	18	Yuan *et al.*[29]
CdS nanoparticles	Chemical bath deposition	17–85	60	30	Demir *et al.*[30]
$BaTiO_3$ nanofiber	Electrospinning	11–95	30	9	Wang *et al.*[31]
Al_2O_3 nanotubes	Precipitation	11–95	10	20	Cheng *et al.*[32]
SnO_2 nanowire	Chemical vapor deposition	30–85	120	20	Kuang *et al.*[33]
Cs_2TeCl_6	Solution growth	5–90	13.8	1.39	Our work

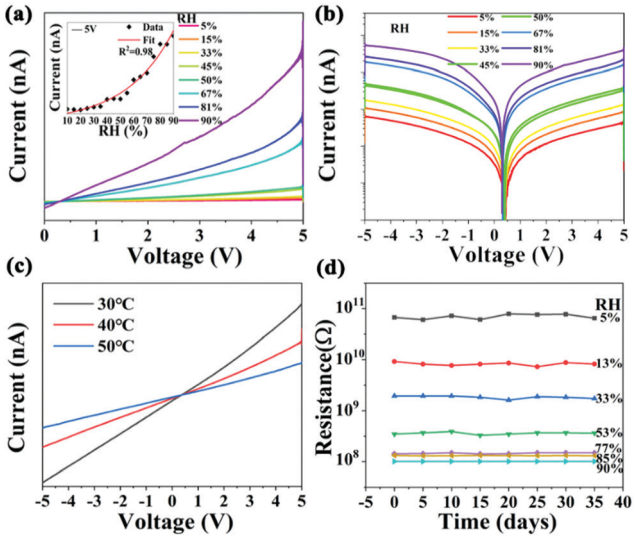

Fig. 3 (a) *I–V* characteristics of the Cs_2TeCl_6-based humidity sensor at different ambient environment RH, the inset plot is the current *versus* RH under 5 V bias. (b) Logarithmic representation of the *I–V* data. (c) *I–V* characteristics of the Cs_2TeCl_6-based sensor recorded at different ambient temperatures (30 °C, 40 °C, and 50 °C, respectively). (d) The long-term stability of the sensor in the air under different RH values.

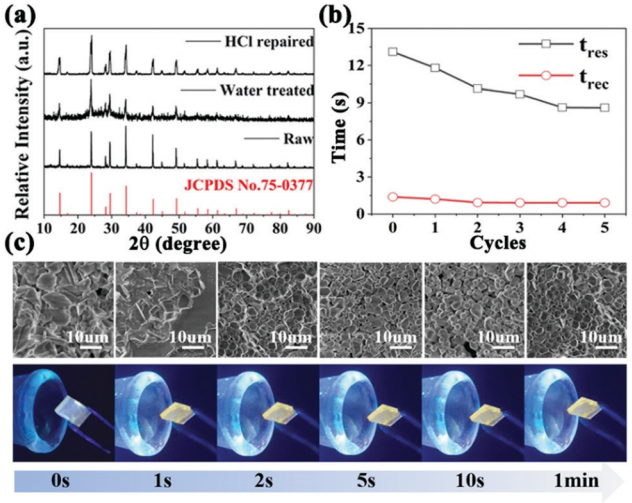

Fig. 4 (a) XRD patterns of Cs_2TeCl_6 before and after the HCl gas treatment. (b) Response and recovery time of the Cs_2TeCl_6-based device before and after multiple cycles of the HCl gas treatment. (c) SEM images and device physical diagram of the sample with different recovery times (0, 1, 2, 5 s, and 1 min).

intensity. Fig. S9 (ESI†) illustrates that the performance of the repaired Cs_2TeCl_6 sensor is far from satisfactory. It is speculated that there is a continuous loss of Cl^{1-} during heat treatment. XPS results shown in Fig. S10 (ESI†) indicate that the peaks located at 573.2 and 576.4 eV are ascribed to $TeCl_4$ and TeO_2, respectively.[38,39] Fig. S11 (ESI†) indicates that during the oxidation process on the surface, the $TeCl_4$ peak was still present on the surface of the sensor when the RH was below 90%. In contrast, once the RH is higher than 90%, only the TeO_2 information could be detected, it will return to the original position after heat treatment, which can be proved from the offset of the binding energy before and after O 1s and Cl 2p repair. The above-mentioned results confirm that a post-heat treatment benefits the recovery of the device performance. Unfortunately, the continuous loss of Cl^{1-} and the destruction of the structure during the heat treatment contribute to an unsatisfied outcome.

To solve the problem of the continuous loss of Cl^{1-} caused by the heat treatment, HCl gas was employed to repair the as-explored humidity sensor (Movie S1, ESI†). As shown in Fig. 4a, the sample returned to its original pure phase of Cs_2TeCl_6 with a broad diffraction peak after the HCl gas repair, which suggests that finer Cs_2TeCl_6 particles are obtained after the HCl gas treatment, as shown in SEM images (Fig. 4c). The characteristic luminescence properties of the HCl gas treated sample presented in Fig. S11 (ESI†) indicate that the PL intensity increases with the prolonged HCl gas treatment, and after 5 s, finally it reaches the initial luminescence intensity. Moreover, we measured the response and recovery time of the device before and after multiple cycles of the HCl gas repair, and the results are shown in Fig. 4b. After the HCl gas repair, the response and recovery time of the humidity-sensitive detector could be recovered. With the increase in the number of HCl gas repair, the response time and recovery time of the detector become less, which could be related to the continuous supply of Cl^{1-} and larger surface over bulk area owing to grain refinement. Furthermore, we compared the morphology of the samples before and after the repair and found that the samples after the HCl gas repair appeared to show grain refinement. The significantly-increased surface of Cs_2TeCl_6 could be the reason for the decrease in the response time and recovery time of the humidity sensor. The XPS spectra illustrated in Fig. S12 and S13 (ESI†) show a raw representation of the original sample without any processing. The main peaks of Cl 2p located at 197.5 and 200.3 eV have binding energy positions moved towards a low binding energy after the device surface contacted with water in air. Moreover, the peaks of O 1s located at 532.5 eV moved to 531.7 eV after water treatment. It is worth noting that the main peaks of Cl 2p and O 1s completely returned to their original peak location after a simple HCl gas repair, demonstrating that HCl gas can completely repair the performance of the humidity sensor and solve the problem of device degradation that cannot be solved by simple heat treatment. This also proves the particularity of the HCl gas repair method.

Herein, the reversible lead-free Cs_2TeCl_6 double perovskite-based sensor was integrated with a commercial face mask to realize the real-time monitor of the respiratory profiles of individuals (Movie S2, ESI†). Normal, deep, and fast breathing can be easily differentiated from the recorded current (Fig. 5d). It was found that the peak currents of all respiration modes gradually increase during the first few exhalation-inhalation cycles. The phenomenon could be explained by the gradual formation of a stable water molecule film and the warming of the sensing layer.[40] Fig. 5a, b and c are the enlarged maps corresponding to normal, deep, and fast breathing. In comparison with the normal one, deep breathing induces a series of much stronger electrical signals with a relatively low frequency,

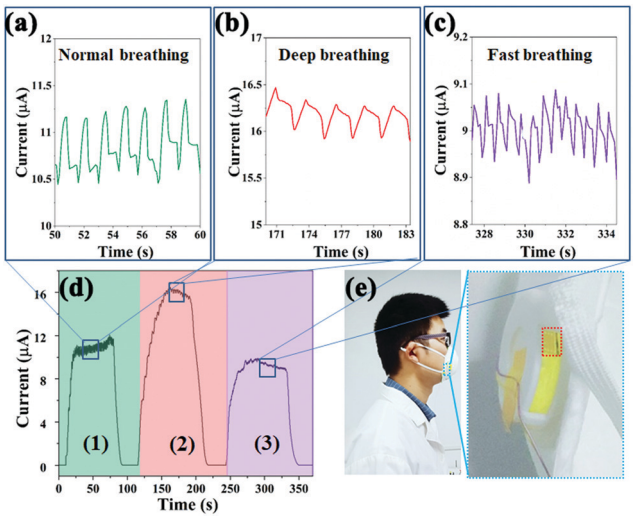

Fig. 5 (a), (b), and (c) are the enlarged response curves corresponding to normal, deep, and fast breathing. (d) Real-time monitor of a normal (1), deep (2), and fast breathing (3) with an integrated Cs_2TeCl_6-based respiration sensor. (e) Schematic of the monitor of human respiration with an electrochemical station.

while along with the deep respiration process, water molecules are exhaled out, leading to a thick water film on the sensing layer. Thus, the resistance of the device remarkably reduces and strong current signals can be detected. Hence, weak electrical responses with a very high frequency are displayed in Fig. 5c. The weak signals could be attributed to two reasons: less moisture from the exhaled air as well as insufficient removal of the adsorbed water layer due to the rapid and shallow breathing.[41] Herein, human respiration could be monitored in real-time by the as-developed sensor, promising wearable electronic devices for clinical respiratory monitoring (Fig. 5e).

Conclusions

In summary, we synthesized a lead-free Cs_2TeCl_6 double perovskite-based humidity sensor. The humidity sensor shows a fast response (13.8 s) and recovery times (1.39 s) in the RH range from 5% to 90%. Moreover, the resistance of the sensor suffered from relatively insignificant change during 35 days of repeated measurements in a relative humidity range of 5% to 90%. Furthermore, the device degradation problem in a high humidity environment (RH > 90%) was fundamentally solved *via* HCl gas repair. Finally, the humidity sensor shows the ability to detect the human respiration rate in real-time, which could be a promising electronic device for clinical respiration monitoring.

Experimental

Materials

Cesium chloride (CsCl, 99.99%) and tellurium dioxide (TeO_2, 99.999%) were purchased from Sigma-Aldrich. Hydrochloric acid (HCl, 37%) and ethanol were purchased from Sinopharm Chemical Reagent Company. All materials were used as received without further purification.

Synthesis of double-perovskite materials

Cs_2TeCl_6 was synthesized according to the procedure reported by Slavney *et al.*[42] In brief, 610 mg CsCl was dissolved in 10 ml of hydrochloric acid in a flask at 60 °C and stirred for 30 min to get precursor A. In another flask, 280 mg TeO_2 was dissolved in 15 ml hydrochloric acid at 90 °C and stirred for 3 h until all solids were dissolved to get the precursor solution B. Then precursor solution A was swiftly injected into the flask containing the precursor solution B and stirred in a sealed glass bottle at 110 °C for 6 h. The solution was centrifuged at 4000 rpm for 8 min. The precipitants were collected and washed with ethanol and dried in a furnace at 60 °C overnight.

Humidity sensor fabrication

Cs_2TeCl_6 were dispersed in absolute ethanol, and 80 μL of the Cs_2TeCl_6 solution was added to the ITO substrate and was spin-coated at 2000 rpm for 30 s to the completion of the spin-coating process. The substrates were subsequently annealed at 150 °C for 30 min to allow the complete formation of the desired double perovskite phase. Finally, the device was completed by evaporating two gold electrodes (50 nm) in a vacuum evaporation-coating equipment.

Material characterization

The powder X-ray diffraction (XRD) patterns of the samples were recorded on a Dandong TD-3500 X-ray diffractometer using Cu Kα radiation, operating at 30 kV and 20 mA. The surface morphology and microstructure of as-obtained products were analyzed on a scanning electron microscope (Hitachi, SU-8010). X-ray photoelectron spectroscopy (XPS) was performed on an ESCA Lab MKII instrument to analyze the chemical composition of the obtained Ni foam. The spectra were recorded using a HITACHI U-4100 UV-vis-NIR spectrophotometer with an integrated sphere in the diffuse-reflectance mode. Samples were prepared by diluting the solution in ethanol in 1 cm path length quartz cuvettes. The PL spectra were taken on a Hitachi F-7000 fluorescence spectrophotometer.

Humidity sensing measurement

The real-time sensing plots and *I–V* curve of Cs_2TeCl_6 thin film humidity sensors were obtained using an electrochemical workstation (CHI 660E, CH Instrument Company, Shanghai, China), which was employed to collect electrical signals by testing amperometric curves of the devices. For the real-time sensing plots, a homemade test system equipped with three channel-valve to switch on the dry air or wet air was fabricated. The gas flow rate was controlled at 15 L min^{-1} and the RH of gas flow was read using a commercial hygrometer (Shandong Renke Co. Ltd, China, Cos-03). HCl gas was used to repair the degraded humidity sensors in a simple and effective way. The details of the HCl gas repair method are shown in the Movie S1 (ESI†). Moreover, we monitored different respiration modes of a

volunteer, including normal, deep, and fast breathing. The detailed test process is shown in the Movie S2 (ESI†).

Theoretical calculation

In this study, the CASTEP module in the Materials Studio software is used to make geometric optimization of Cs_2TeCl_6, and Perdew–Burke–Ernzerhof (PBE) method in General gradient approximation (GGA) was used to calculate its electronic structure. In the calculation, the plane wave truncation energy was selected to be 550 eV, and the Brillouin region integral was adopted to be an inverse lattice space of $2 \times 2 \times 2$ k points, and the convergence value of the total energy of each atom was 1.0×10^{-5} eV.

Conflicts of interest

There are no conflicts to declare.

Acknowledgements

This work was financially supported by National Nature Science Foundation of China (NSFC) (61965012, 11664022), the Reserve talents project of Yunnan Province (2017HB011), Yunnan Ten Thousand Talents Plan Young & Elite Talents Project (YNWR-QNBJ-2018-295, YNWR-QNBJ-2018-325), the Excellent Youth Project of Yunnan Province Applied Basic Research Project (2019FI001), foundation of Yunnan Province (2019HC016), National Science Funds of China (Grant No. 12064022), and China Postdoctoral Science Foundation (2019M663575).

Notes and references

1 C. Zhou, X. Zhang, N. Tang, Y. Fang, H. Zhang and X. Duan, *Nanotechnology*, 2020, **31**, 125302.
2 J. Zhao, B. Cai, Z. Luo, Y. Dong, Y. Zhang, H. Xu, B. Hong, Y. Yang, L. Li and W. Zhang, *Sci. Rep.*, 2016, **6**, 21976.
3 Y.-Y. Zhang, S. Chen, P. Xu, H. Xiang, X.-G. Gong, A. Walsh and S.-H. Wei, *Chin. Phys. Lett.*, 2018, **35**, 036104.
4 D. Zhang, H. Chang, P. Li, R. Liu and Q. Xue, *Sens. Actuators, B*, 2016, **225**, 233–240.
5 J. S. Yun, J. Kim, T. Young, R. J. Patterson, D. Kim, J. Seidel, S. Lim, M. A. Green, S. Huang and A. Ho-Baillie, *Adv. Funct. Mater.*, 2018, **28**, 1705363.
6 M. Yuan, Y. Zhang, X. Zheng, B. Jiang, P. Li and S. Deng, *Sens. Actuators, B*, 2015, **209**, 252–257.
7 P. Yasaei, A. Behranginia, T. Foroozan, M. Asadi, K. Kim, F. Khalili-Araghi and A. Salehi-Khojin, *ACS Nano*, 2015, **9**, 9898–9905.
8 J. Yang, B. D. Siempelkamp, D. Liu and T. L. Kelly, *ACS Nano*, 2015, **9**, 1955–1963.
9 W. Xu, F. Li, Z. Cai, Y. Wang, F. Luo and X. Chen, *J. Mater. Chem. C*, 2016, **4**, 9651–9655.
10 Z. Weng, J. Qin, A. A. Umar, J. Wang, X. Zhang, H. Wang, X. Cui, X. Li, L. Zheng and Y. Zhan, *Adv. Funct. Mater.*, 2019, **29**, 1902234.
11 Y. Wang, R. W. Besant, C. J. Simonson and W. Shang, *Sens. Actuators, B*, 2006, **115**, 93–101.
12 L. Wang, Y. He, J. Hu, Q. Qi and T. Zhang, *Sens. Actuators, B*, 2011, **153**, 460–464.
13 M. A. Squillaci, L. Ferlauto, Y. Zagranyarski, S. Milita, K. Müllen and P. Samorì, *Adv. Mater.*, 2015, **27**, 3170–3174.
14 A. H. Slavney, T. Hu, A. M. Lindenberg and H. I. Karunadasa, *J. Am. Chem. Soc.*, 2016, **138**, 2138–2141.
15 J. A. Schwenzer, L. Rakocevic, R. Gehlhaar, T. Abzieher, S. Gharibzadeh, S. Moghadamzadeh, A. Quintilla, B. S. Richards, U. Lemmer and U. W. Paetzold, *ACS Appl. Mater. Interfaces*, 2018, **10**, 16390–16399.
16 C. Rubinger, C. Martins, M.-A. De Paoli and R. Rubinger, *Sens. Actuators, B*, 2007, **123**, 42–49.
17 K. Ren, L. Huang, S. Yue, S. Lu, K. Liu, M. Azam, Z. Wang, Z. Wei, S. Qu and Z. Wang, *J. Mater. Chem. C*, 2017, **5**, 2504–2508.
18 B. W. Park and S. I. Seok, *Adv. Mater.*, 2019, **31**, 1805337.
19 Y. Pang, J. Jian, T. Tu, Z. Yang, J. Ling, Y. Li, X. Wang, Y. Qiao, H. Tian and Y. Yang, *Biosens. Bioelectron.*, 2018, **116**, 123–129.
20 U. Mogera, A. A. Sagade, S. J. George and G. U. Kulkarni, *Sci. Rep.*, 2014, **4**, 4103.
21 W. Ming, S. Chen and M.-H. Du, *J. Mater. Chem. A*, 2016, **4**, 16975–16981.
22 B. Li, G. Xiao, F. Liu, Y. Qiao, C. M. Li and Z. Lu, *J. Mater. Chem. C*, 2018, **6**, 4549–4554.
23 C.-W. Lee, H.-S. Park, J.-G. Kim, B.-K. Choi, S.-W. Joo and M.-S. Gong, *Sens. Actuators, B*, 2005, **109**, 315–322.
24 Q. Kuang, C. Lao, Z. L. Wang, Z. Xie and L. Zheng, *J. Am. Chem. Soc.*, 2007, **129**, 6070–6071.
25 D. Kou, W. Ma, S. Zhang, J. L. Lutkenhaus and B. Tang, *ACS Appl. Mater. Interfaces*, 2018, **10**, 41645–41654.
26 H. Konno and Y. Yamamoto, *Bull. Chem. Soc. Jpn.*, 1988, **61**, 2990–2992.
27 A. Jia, B. Liu, H. Liu, Q. Li and Y. Yun, *Front. Chem.*, 2020, **8**, 383.
28 Z. Imran, S. Batool, H. Jamil, M. Usman, M. Israr-Qadir, S. Shah, S. Jamil-Rana, M. A. Rafiq, M. Hasan and M. Willander, *Ceram. Int.*, 2013, **39**, 457–462.
29 L. Hu, G. Shao, T. Jiang, D. Li, X. Lv, H. Wang, X. Liu, H. Song, J. Tang and H. Liu, *ACS Appl. Mater. Interfaces*, 2015, **7**, 25113–25120.
30 Y. Han, S. Meyer, Y. Dkhissi, K. Weber, J. M. Pringle, U. Bach, L. Spiccia and Y.-B. Cheng, *J. Mater. Chem. A*, 2015, **3**, 8139–8147.
31 C. D. Flint and A. G. Paulusz, *Inorg. Chem.*, 1981, **20**, 1768–1771.
32 R. H. Fang, A. V. Kroll, W. Gao and L. Zhang, *Adv. Mater.*, 2018, **30**, 1706759.
33 G. Divitini, S. Cacovich, F. Matteocci, L. Cinà, A. Di Carlo and C. Ducati, *Nat. Energy*, 2016, **1**, 1–6.
34 M. R. Detty, W. C. Lenhart, P. G. Gassman and M. R. Callstrom, *Organometallics*, 1989, **8**, 861–865.

35 R. Demir, S. Okur and M. E. Şeker, *Ind. Eng. Chem. Res.*, 2012, **51**, 3309–3313.
36 B. Conings, J. Drijkoningen, N. Gauquelin, A. Babayigit, J. D'Haen and L. D'Olieslaeger, *Adv. Energy Mater.*, 2015, **5**, 1.
37 B. Cheng, B. Tian, C. Xie, Y. Xiao and S. Lei, *J. Mater. Chem.*, 2011, **21**, 1907–1912.
38 Y. Chen, X. Ma, C. Li, Q. Wu, Y. Wang, M. Huang, B. Liu and L. Li, *Int. J. Mod. Phys. B*, 2020, **34**, 2040003.
39 Y. Chen, C. Li, X. Ma, Q. Qiang, B. Liu, S. Cao, L. Peng, L. Li and T. Lang, *Appl. Surf. Sci.*, 2020, **506**, 144816.
40 J. Bisquert and E. J. Juarez-Perez, *The Causes of Degradation of Perovskite Solar Cells*, ACS Publications, 2019.
41 K. P. Biju and M. K. Jain, *Sens. Actuators, B*, 2008, **128**, 407–413.
42 D. Bauskar, B. Kale and P. Patil, *Sens. Actuators, B*, 2012, **161**, 396–400.